ELSEVIER

Contents lists available at ScienceDirect

### Journal of Fluids and Structures

journal homepage: www.elsevier.com/locate/jfs



## Comparison of experimental and numerical studies on the flow structures of hovering hawkmoths



Yun Liu<sup>a,\*</sup>, Angel David Lozano<sup>a</sup>, Tyson L. Hedrick<sup>b</sup>, Chengyu Li<sup>c</sup>

- <sup>a</sup> Department of Mechanical and Civil Engineering, Purdue University Northwest, Westville, IN 46323, USA
- b Department of Biology, University of North Carolina at Chapel Hill, Chapel Hill, NC 27599, USA
- <sup>c</sup> Department of Mechanical Engineering, Villanova University, Villanova, PA 19085, USA

#### ARTICLE INFO

# Article history: Received 20 April 2021 Received in revised form 12 September 2021 Accepted 23 September 2021 Available online xxxx

Keywords: Insect flight Wake flow structures Schlieren photography CFD simulation

#### ABSTRACT

This study presents an effort on comparing the wake flow structures of hovering insects between experimental visualization and computational simulation. The wake flow on a freely hovering hawkmoth was visualized and captured, utilizing a high-speed schlieren photography system with isopropyl alcohol brushed on the wing surfaces. Meanwhile, an Immersed Boundary Method (IBM) based computational fluid dynamics (CFD) simulation was carried out on a hovering hawkmoth to resolve the entire flow field. On each wing of the hovering hawkmoths, both the schlieren photography experiment and the CFD simulation captured and visualized very alike wake structures, consisting of a vortex loop structure in the down-stroke and tip/root vortices in the up-stroke. Furthermore, the experiment and simulation results are compared by measuring the sizes of the vortex structures. The agreement in flow structure formation and its size between the experiment and simulation suggests that the implemented IBM-based CFD simulation method is capable of simulating the actual flow phenomena on the hovering insect with valid flow structure details such as flow structure size. On the other hand, our study confirms the high-speed schlieren photography's capability of capturing the wake flow structures formation, which is challenging to resolve with other methods.

© 2021 Published by Elsevier Ltd.

#### 1. Introduction

Over the past decades, with the advancement of Experimental Fluid Dynamics (EFD) and Computational Fluid Dynamics (CFD) techniques, on flying insects/hummingbirds, new details about the flow structures and new aspects of aerodynamic forces have been discovered and recognized (Ellington et al., 1996; Birch and Dickinson, 2001; Warrick et al., 2005; Bomphrey et al., 2006; Altshuler et al., 2009; Pournazeri et al., 2013; Henningsson et al., 2015; Liu et al., 1998; Aono et al., 2008; Shyy et al., 2010; Nakata and Liu, 2012; Li et al., 2018a; Bomphrey et al., 2017). Utilizing the smoke/smoke wire visualization on tethered hawkmoth as well as a hawkmoth mimicking mechanical flapper, a cone-shaped leading edge vortex (LEV) was revealed, leading to an important recognition of lift augmenting mechanics of flying insects (Ellington et al., 1996). In addition to the qualitative visualization, quantitative Digital Particle Image Velocimetry (DPIV) has been extensively used in studying the unsteady flow on flying insects/hummingbirds, revealing a complex flow field (Birch and Dickinson, 2001; Warrick et al., 2005; Bomphrey et al., 2006; Altshuler et al., 2009). However, the majority of these studies were limited to either the qualitative flow visualization on regional flow structures or quantitative flow field

E-mail address: liu739@pnw.edu (Y. Liu).

<sup>\*</sup> Corresponding author.

measurements on two-dimensional planes, whereas, the actual flow structures on hovering insects/hummingbirds are highly three-dimensional and unsteady (Sane, 2003). Therefore, inferring the full three-dimensional flow structure on hovering animals from conventional flow visualization and measurement is quite challenging and impractical. Recent advances in three-dimensional flow reconstruction and particle tracking algorithms enabled the flow measurement on flapping wings in all the three dimensions (Henningsson et al., 2015; Kim and Gharib, 2010; Liu et al., 2013; Cheng et al., 2014; Schanz et al., 2016). Recently, a volumetric Tomographic PIV experiment was conducted in the wake below hovering hummingbird hawkmoths, capturing series of bilateral, stacked vortex rings (Varfvinge et al., 2021). The induced power was estimated from the measured flow field and compared with the theoretical model. However, the Tomographic PIV only enabled three-dimensional flow measurement and visualization in the far-field wake region, away from the wings, leaving the near wake three-dimensional unsteady flow and its associated aerodynamic performance still unclear (Varfvinge et al., 2021).

On the other hand, in spite of the challenges imposed from the complex wing geometries and motions, the complex 3D unsteady flow on hovering insects/hummingbirds has been extensively studied numerically. Initially, to accommodate the complexities of reciprocating flapping wing motions and wing geometries, the computational mesh was updated at each iteration and the boundary-conforming methods were implemented (Liu et al., 1998). Later, by introducing the immersed boundary method (IBM), in which stationary non-body conformal Cartesian grids could be implemented, the computational cost of simulating the flow on flapping wings was significantly reduced (Mittal and Iaccarino, 2005b). Paired with the wing kinematics data extracted from actual flying insects, over the past decade, complex flow structures on different insect species under different flight conditions were extensively simulated and studied numerically, revealing unprecedented details about the flow structures and aerodynamic forces (Mittal et al., 2008; Wang et al., 2019; Li and Dong, 2017a; Liu et al., 2016; Wan et al., 2015). However, as conventional experimental techniques could not capture and measure the entire three-dimensional flow structure and flow field, the simulated flow field results were rarely validated and compared with the experimental flow field data on freely flying insects/hummingbirds, other than two dimensional flow field data on specific planes or the total force measurement data.

The lack of full flow field measurement/visualization on freely flying insects/hummingbirds leads to several consequences. First, although the CFD simulations on flying insects/hummingbirds have been validated and compared with experiments on two dimensional plans or in force measurements, the CFD simulation results have never been compared with the experiments in a full flow field scope. Therefore, considering the accuracy of the input wing morphology and kinematics data as well as the effect of small scale textures/features on the insect/hummingbird wing surfaces, it is unclear if all the numerical simulations can truthfully reflect the actual flow phenomena and physics. Second, a thorough understanding about the full flow field/structure is important to the interpretation of unsteady aerodynamic mechanisms on flying insects/hummingbirds. In the absence of such knowledge, current understanding about the aerodynamics of flying insects/hummingbirds is primarily limited to local and static aerodynamic mechanisms. For instance, the local flow structure of leading edge vortex is widely considered as the major mechanism of aerodynamic force generation/augmentation and has been extensively investigated experimentally (Ellington et al., 1996; Bomphrey et al., 2006, 2009; Muijres et al., 2008; Viderler et al., 1996; Jardin, 2017; Chen et al., 2020). However, in most studies, only the instantaneous/static flow of the LEV is considered and correlated to lift generation while other flow features, like the starting vortex and transient behavior of the flow, are quite often ignored. On a scaled-up robotic flapper that could mimic the complex flapping wing motion of a hovering hawkmoth, however, Van Den Berg and Ellington successfully visualized the full flow field and captured two vortex rings, one per wing, during the down-stroke. Furthermore, the size and kinematics of the vortex ring were investigated systematically to perceive the underlying unsteady aerodynamics, substantiating the significance of knowing the full flow structure and its behavior (van den Berg and Ellington, 1997).

Recently, a high-speed schlieren photography was implemented on a freely flying hawkmoth with isopropyl alcohol brushed on the wing surfaces, capable of visualizing the full wake flow (Liu et al., 2018). With the alcohol vapor released from wing surfaces and a unity Schmidt number, the alcohol vapor accurately traces the vortical flow structures which were successfully captured by the schlieren systems from two orthogonal views. In this paper, the vortex structures in the wake of a hovering hawkmoth will be three-dimensionally reconstructed from a schlieren photography experiment. Meanwhile, an IBM method based numerical simulation will be performed on a hovering hawkmoth to achieve a comprehensive flow field comparison between the experiment and simulation.

#### 2. Materials and methods

#### 2.1. High speed schlieren photography and structure reconstruction

Utilizing the high-speed schlieren photography, the overall vortex structures on a freely flying hawkmoth *Manduca* (1.26 g, wing span length of 4.1 cm) were captured and visualized (Liu et al., 2018). The experiment setup consists of two single mirror, double-pass, schlieren photography systems with two high speed cameras (Mini UX100, Photron), filming the flow field from two orthogonal views. For each schlieren photography setup, the light was created from a white LED through a 1 mm pin hole and was projected on a 10-inch diameter concave spherical mirror (Edmond Optics). Then a 50/50 (reflection/transmission ratio, Edmond optics) beam-splitter was utilized to direct the reflected light from the mirror to the high speed camera while a vertical razor blade was implemented at the focal point to produce schlieren imaging

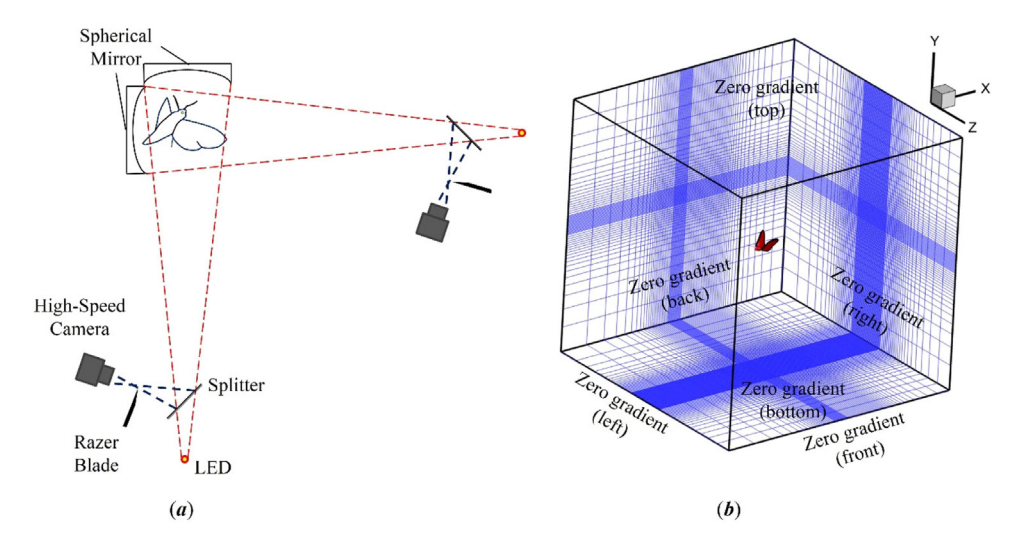


Fig. 1. (a) Schlieren photograph setup. (b) Computational grids for numerical simulation.

(Fig. 1a). In the beginning of the experiments, an  $8\times8\times6$  inches calibration target was filmed by the two high speed cameras for flow structure reconstruction. To visualize the vortex structures from freely flying insects, before testing, warm isopropyl alcohol (91% Isopropyl Alcohol heated to 38 °C) was brushed onto the surface of the wings then the hawkmoth was released to fly freely in the flow observation region. During the free flight, the airflow over the wing surface increases vaporization of the alcohol, drawing it into the vortical flow created from the flapping wings. Taking the diffusion coefficient of isopropyl alcohol in air to be 0.1011 cm  $^2$ /s, the Schmidt number of vaporized median is estimated to be at the order of one, therefore alcohol vapor should accurately reflect the vortical flow structures formation (Smits and Lim, 2012). Consequently, the unsteady three-dimensional vortex structure was visualized and recorded by the high speed cameras at 1000 frames per second. Then, a direct linear transformation (DLT) method implemented in the MATLAB program DLTdv7 (Hedrick, 2008) can be applied to the schlieren images to reconstruct the outlines of vortex structures in three dimensions (3D). First, the images of the calibration target were utilized to generate the calibration coefficients for direct linear transformation. Then the vortex structures are digitally outlined on the schlieren images filmed from two orthogonal views. Finally, with the DLT calibration coefficients, the vortex loop outlines can be reconstructed in 3D.

#### 2.2. Direct numerical simulation of hovering hawkmoth

The hawkmoth hovering motion recorded and reconstructed in the CFD study was a male *Mandua sexta* (1.45 g body mass and 5.11 cm wing span) from the colony at The University of North Carolina at Chapel Hill. The moth exhibit controlled hovering flight behavior when feeding from an artificial flower containing a sugar solution. To capture the essential anatomical and geometric features of the hovering animals, Autodesk Maya was used to construct the unstructured mesh surfaces of hawkmoth body and wings. A template model was generated using Catmull–Clark subdivision surfaces which allow further refinement of the surface representations by recursively repeating the subdivision algorithm. Based on the image sequences captured by high-speed cameras from the experiment, we can align the vertices of the subdivision surface hierarchy according to the geometric shape and natural pattern of the hovering hawkmoth's body and wings. Thus, the dynamic motion can be iteratively mapped onto the subdivision surface model, thereby providing an in vivo representation of the flying motion.

After the refinement of the model in both space and time, the reconstructed hovering motion was used as the input data for the in-house immersed-boundary-method-based CFD solver. The governing equations of airflow for insect flight are the unsteady incompressible viscous Navier–Stokes equations. The non-dimensional form of the governing equations is shown in Eq. (1), and discretized using the collocated grid arrangement, where the primitive variables ( $u_i$  and p) are stored in the cell center. The equations are integrated with time using the fractional step method and a second-order central difference scheme in space is employed. A sharp interface immersed boundary method is adopted for handling the complex moving boundaries involved in flapping motion. The complex immersed wing and body surfaces are represented by unstructured triangular elements, while the flow is computed on the Cartesian grids. The boundary conditions on the immersed boundaries are imposed through a ghost-cell procedure. The current numerical treatment can eliminate the need for the mesh regeneration at each time step, and thus save the computational cost. This in-house flow solver has been successfully applied to study canonical flapping propulsion problems (Li and Dong, 2016; Li, 2020) and insect flight

**Table 1**Morphological data for the hawkmoths used in CFD simulation and schlieren photography experiment.

	Wing span	Mean wing chord	Flapping	Wing stroke	Body	Reynolds
	length (cm)	length (cm)	frequency (Hz)	Amplitude (rad)	mass (g)	number
CFD	5.1	2.56	26.3	1.75	1.45	7700
EXP	4.1	2.85	22.7	1.90	1.26	6500

(Li et al., 2018; Li and Dong, 2017b). The validations of this solver can be found in the author's previous papers (Li et al., 2015, 2017).

$$\frac{\partial u_i}{\partial x_i} = 0, \quad \frac{\partial u_i}{\partial t} + \frac{\partial (u_i u_j)}{\partial x_j} = -\frac{\partial p}{\partial x_i} + \frac{1}{Re} \frac{\partial}{\partial x_j} (\frac{\partial u_i}{\partial x_j})$$
(1)

where  $u_i$  represents three velocity components in the Cartesian coordinate system, p is the pressure, and Re is the Reynolds number. In the current study, the Reynolds numbers are calculated with the following equation (2), where  $\Phi$  represents the stroke amplitude, n stands for flapping frequency, S stands for wing span length,  $\overline{C}$  stands for mean chord length and v is the kinematic viscosity. Table 1 summarize the physical parameters of the tested hawkmoths in the CFD simulation and schlieren photography experiment.

$$Re = \frac{2\Phi nS\overline{C}}{v} \tag{2}$$

#### 3. Results

#### 3.1. Vortex structure comparison

Fig. 2 presents the comparison of vortex structures between the schlieren photography and the CFD simulation. Fig. 2a and Fig. 2d present the schlieren photography images in the down-stroke and up-stroke from two different wing beat cycles where the vortex structures can be seen from better perspectives. Fig. 2b and Fig. 2e show the numerically simulated 3D flow field, which is visualized from the iso-surface of Q-criterion.

After the wing pronation of each wing, in both the schlieren photography and CFD simulation, a combined structure of starting and stopping vortex (SV) is visualized (Fig. 2a). Then very quickly, significant tip and root vortex are formed from the tip and root of the wing while a stable leading-edge vortex (LEV) is created with one end connecting to the tip vortex (Fig. 2c). Therefore, in the down-stroke, both the schlieren photography and CFD simulation captured a similar loop structure that connects leading-edge vortex (LEV), tip vortex (TV), starting/stopping vortex (SV) and root vortex (RV) together. However, in addition to the fore-wing tip vortex  $(TV^1)$ , the schlieren photography captured a secondary tip vortex (TV<sup>2</sup>) from the hind-wing whereas the CFD simulation only captures the fore-wing tip vortex in the downstroke. In our CFD simulation, the fore-wing and hind-wing had to be combined as a single surface in order to obtain converged simulation results. However, for a real moth, the fore-wing and hind-wing are separate structures and not always perfectly aligned during the flapping motion. This CFD treatment potentially caused the inconsistency between the schlieren photography and CFD simulation on the secondary tip vortex from the hind-wing. In the up-stroke, schlieren photography and the CFD simulation results show better agreement, capturing elongated tip and root vortices with ends connecting to the shed vortex structure from the down-stroke. In addition to capturing the root and fore-wing tip vortex, the CFD simulation also resolved the secondary hind-wing tip vortex (TV<sup>2</sup>) that is revealed in the schlieren photography. Therefore, after one complete wing beat cycle, both the CFD simulation and the schlieren photography capture very similar vortex structures that consist of a vortex loop in the far wake, two tip vortices and a root vortex in the near field.

#### 3.2. Vortex size comparison

To have a further comparison, the vortex structure size is extracted and compared between the schlieren photography and CFD simulation. In the down-stroke, the vortex loop structure, consisting of the leading-edge vortex, fore-wing tip vortex, starting/stopping vortex and root vortex, is outlined and reconstructed three-dimensionally from the high-speed schlieren photography images, utilizing the direct linear transformation (DLT) method implemented in the MATLAB program DLTdv7 (Hedrick, 2008). Similarly, in the up-stroke, the tip and root vortex structures are outlined and reconstructed three-dimensionally from the schlieren images. As the vortex structures are close to the insect wings/body and cannot be reconstructed if they are blocked on the schlieren photography images, only ten consecutive pairs of schlieren images of vortex loops in the down-stroke and eleven consecutive pairs of schlieren images of tip and root vortices in the up-stroke captured the entire desired structures and are ultimately utilized in the 3D reconstructions.

Fig. 3a I and Fig. 3a II present an example of schlieren image pair used for reconstructing the vortex loop structure in the down-stroke at t = 0.32 T (T is the duration of one wing beat cycle). The red dot lines present the outlines of the vortex loop. Fig. 3a III shows the reconstructed vortex loops from the ten consecutive pairs of the schlieren images from t = 0.32 T (T is the duration of one wing beat cycle).

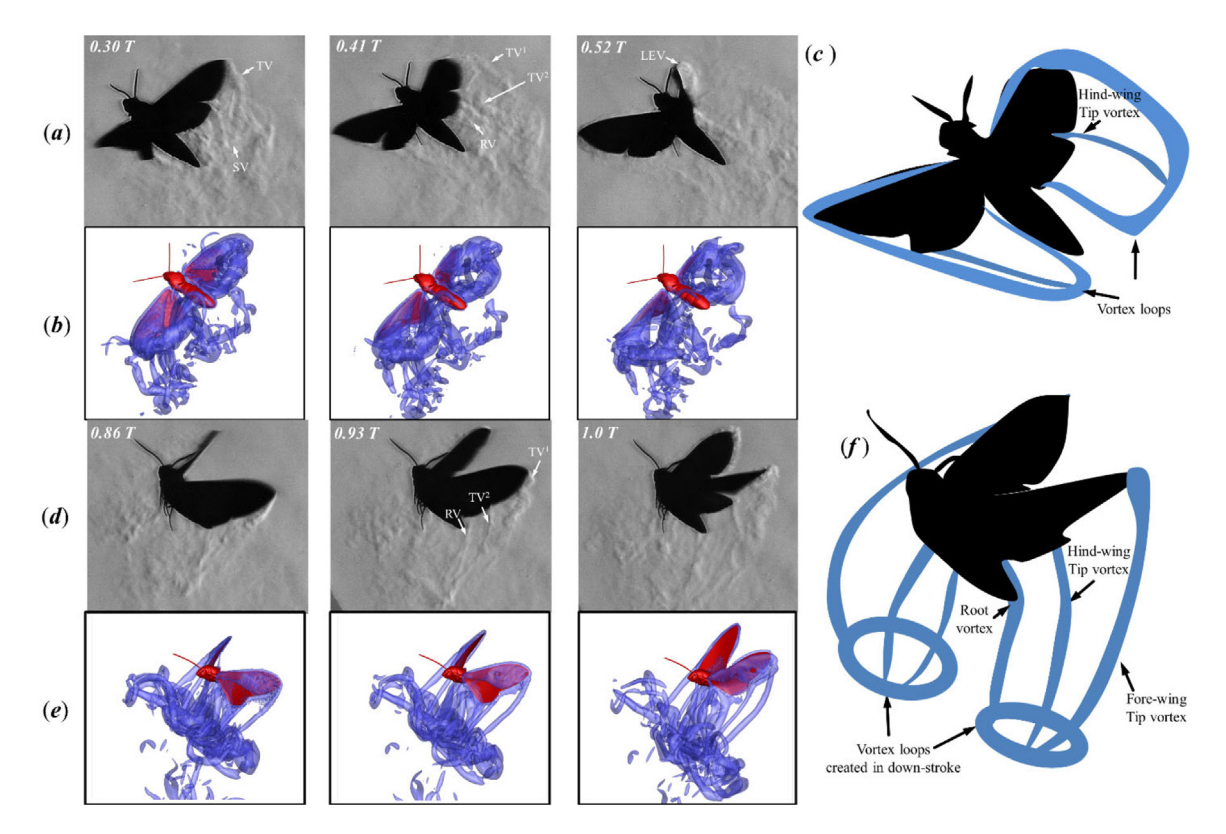


**Fig. 2.** Comparison of flow structures between schlieren photography (Liu et al., 2018) and CFD simulation. (a) schlieren photography results during the down-stroke. (c) Sketch of vortex structures on a hovering hawkmoth in the down-stroke. (d) schlieren photography results in the up-stroke. (e) CFD simulation results in the up-stroke. (f) Sketch of vortex structures on a hovering hawkmoth in the up-stroke. The vortex structure of CFD simulation is shown by the iso-surface of Q = 140.

0.25 T to t=0.45 T. The blueish curves indicate the vortex loops created in the early time instants while reddish curves represent vortex loops formed in the later time. As the wing sweeps, the vortex loop extends and convects, resulting a continuously enlarging loop structure. Similarly, in the up-stroke, the tip vortices created from the tips of the foreand hind-wings as well as the root vortices are outlined in schlieren images. Fig. 3b I and Fig. 3b II display an example of schlieren image pair that is used for tip and root vortex structure reconstruction at t=0.95 T (The red dot lines indicate the outlines of the tip and root vortices). Fig. 3b III presents the resulting three-dimensional tip and root vortex reconstructed from the eleven consecutive pairs of schlieren images in the up-stroke from t=0.77 T to t=1.0 T. (Time evolves from the blue to red). During the up-stroke, the wing sweeps up and backward, creating elongated vortex tubes from the tips and root of the wing.

In total, five sets of three-dimensional reconstructions were conducted for the selected pairs of schlieren images. The reconstructed vortex structures from the schlieren images are then projected on three orthogonal planes of the coordinate system: XY, XZ, YZ planes, (the coordinate system is determined by the calibration target that is used in the beginning of the experiments) to measure the areas enclosed by the vortex structures. Meanwhile, the projected areas are divided by the square of the wing span length (measured from the wing tip to the root) to derive the dimensionless area. Fig. 4. a displays the time history of three dimensionless projected areas from the formed vortex loop in the down-stroke. The error bar is provided from calculating the standard deviation of the five sets of 3D reconstructions. The dimensionless vortex loop areas on YZ and XZ planes (red and green) increase continually and dominate the vortex loop size variation while the dimensionless vortex loop area on XY plane (blue) has much smaller value and less contribution to the overall vortex loop size variation. However, the projected areas are heavily dependent on the choice of coordinate system, thus the total area |A| of the vortex loop structure is estimated using Eq. (3) to quantify the overall size of the vortex structure.

$$|\mathbf{A}| = (A_{XY}^2 + A_{XZ}^2 + A_{YZ}^2)^{\frac{1}{2}} \tag{3}$$

The resulting total dimensionless area |A| of the vortex loop structure increases rapidly from 0.71 to 1.51 over the time of measurement (0.25 T < t < 0.45 T), substantiating the observation on the expanding vortex loop in the schlieren images. Likewise, the enclosed areas by the tip and root vortex in the up-stroke can be analyzed in a similar way. In the up-stroke, two regions are formed with one by the hind- and fore-wing tip vortices (region I in Fig. 3b III) and another one by the

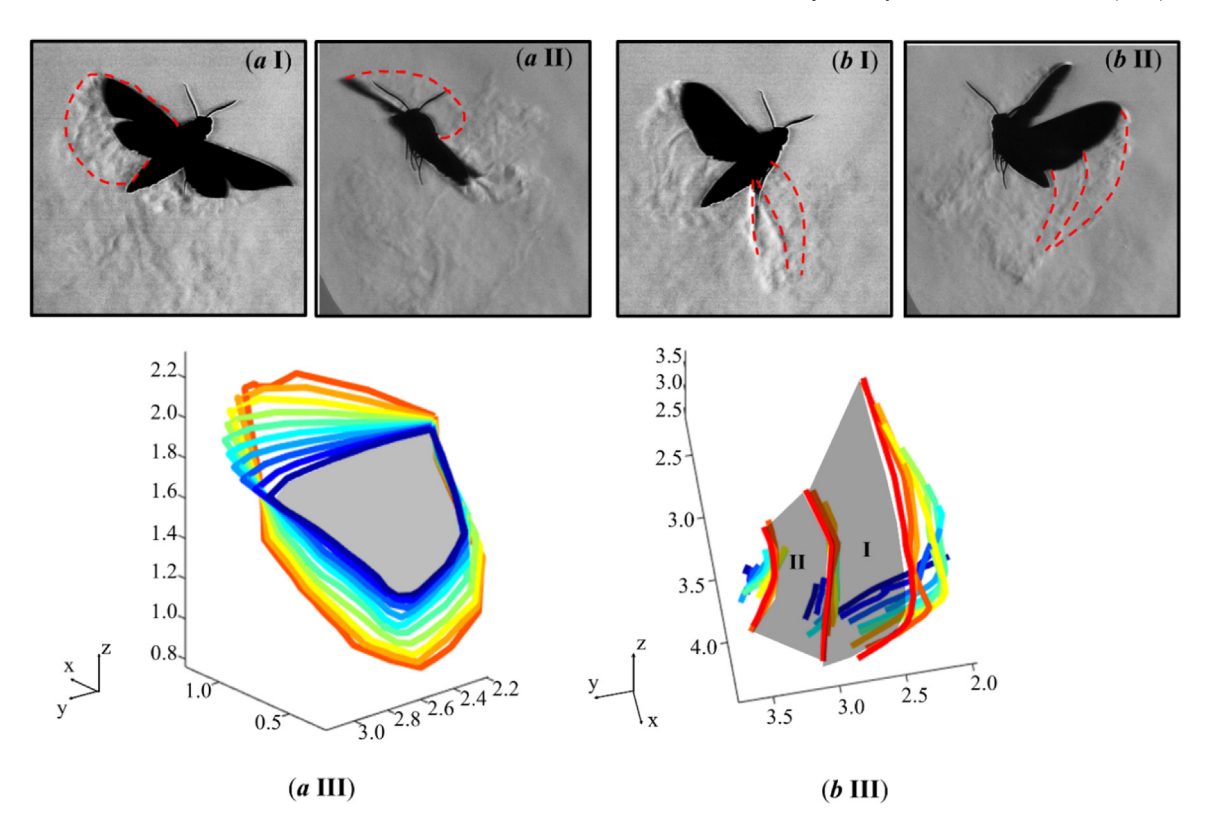


**Fig. 3.** Three-dimensional vortex structure reconstruction from schlieren photography images. (a I, a II) a pair of schlieren image sample used in the down-stroke vortex structure reconstruction at t=0.32 T. (a III) reconstructed vortex loops in down-stroke from t=0.25 T to t=0.45 T. (a II) a pair of schlieren image sample used in the up-stroke vortex structure reconstruction at t=0.95 T. (a III) reconstructed root and tip vortices in the up-stroke from t=0.77 T to t=1.0 T. The blueish curves indicate the vortex filament created in the early time instants while reddish curves represent vortex filament formed in the later time.

root and hind-wing tip vortex (region II in Fig. 3b III). Moreover, at the end, the structures are connected to the wings and vortex structures from the down-stroke, forming two enclosed loops. Subsequently, the projected dimensionless areas of the enclosed region I and II are evaluated and plotted in Fig. 4c. As the projected areas of the enclosed loop structure only reflect the sizes of the vortex structure from one of the three perspectives, similar to the analysis on the vortex loop structure in the down-stroke, the total dimensionless areas of the vortex structures in the up-stroke are calculated and presented in Fig. 4d. The total dimensionless area of the region enclosed by hind- and fore-wing tip vortices is considerably larger than the one region enclosed by the root and hind-wing tip vortices, while both sizes of the structures increase over the most of the time in the up-stroke (0.77 T < t < 1.0 T), depicting elongating root and tip vortices during the up-stroke. Yet, compared to the size of the vortex loop structure in the down-stroke, the enclosed structures in the up-stroke are much smaller and expand slowly. The total dimensionless area of the enclosed region I (hind- and fore-wing tip vortices) increased from 0.16 to 0.44 while the one of enclosed region II (root and hind-wing tip vortices) increased from 0.01 to 0.28 over the time of measurement in the up-stroke (0.77 T < t < 1.0 T).

On the other hand, the sizes of the vortex structures from the CFD simulation are analyzed and estimated. Fig. 5 displays the CFD simulated vortex structures in the down- and up-strokes with the vortex structures visualized at the Q = 140. Fig. 5a, b, c present the vortex loop structure formed in the down-stroke (t = 0.45 T) with its projections on YZ, XZ, XY planes. Fig. 5d, e, f present the tip and root vortices created in the up-stroke (t = 1.0 T) with their projections on YZ, XZ, XY planes. Then in a MATLAB program, the areas of these structure projections are estimated by outlining the corresponding vortex structure projections to quantify the sizes of the CFD simulated vortex structures. Similar to the area quantification of vortex structure in schlieren photography, the areas of the simulated vortex structure projections are estimated five times to quantify the uncertainty.

Fig. 6a, and c present the estimated dimensionless areas of the vortex structure projections from the CFD simulations in the down- and up-stroke. In Fig. 6a, the areas of the down-stroke vortex loop projection on XZ and YZ planes continually increase while the projection area on XY plane first decreases and then increase. However, as the coordinate systems are different between the CFD simulation and schlieren photography experiments, where the Y axis defines the vertical direction in CFD simulation but Y axis is inclined in space in schlieren experiments, the projection areas on individual plane are not comparable. Total area estimations, however, are independent of the specific coordinate system and are thus

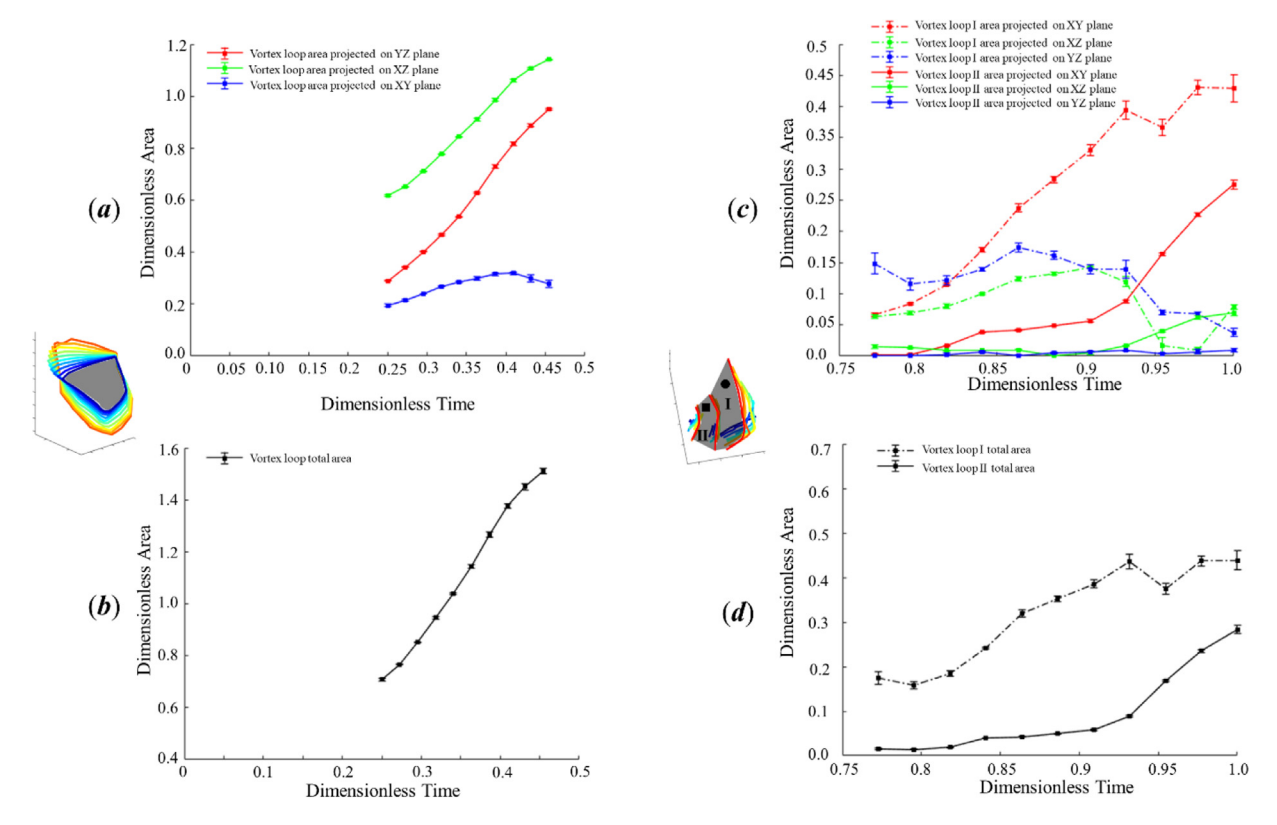


**Fig. 4.** Dimensionless areas of reconstructed vortex structures from schlieren images. (a) Dimensionless areas of down-stroke vortex loop projected on YZ, XZ, XY planes. (b) Total dimensionless area of the down-stroke vortex loop structures. (c) Dimensionless areas of region I (edged on tip vortices from the hind- and fore-wing tips) projected on YZ, XZ, XY planes and dimensionless areas of region II (edged on root and hind-wing tip vortices) projected on YZ, XZ, XY planes. (d) Total dimensionless areas of region II in the up-stroke.

comparable among schlieren and CFD results. Consequently, the total area of the vortex structures in CFD simulations are estimated and plotted in black curves in Fig. 6b and d while the total areas of vortex structures from schlieren experiment are replotted in gray curves for comparison.

In general, the CFD simulation and schlieren photography results have a good agreement on the vortex size and development trend. In the down-stroke, both the CFD simulation and schlieren photography experiment reveal an enlarging vortex loop structure over the time of measurement with the total dimensionless area increased from 0.71 to 1.51 in schlieren experiment versus total dimensionless area increased from 0.83 to 1.27 in CFD simulation. Yet the captured vortex loop structure in the schlieren experiments clearly grows more rapidly, compared to the CFD simulation. In the up-stroke, both the CFD simulation and schlieren photography captured the elongating root and tip vortices. The enclosed region I is formed by two vortices shed from the tips of fore- and hind-wings and the enclosed region II is formed by the vortices from the tip of hindwing and wing root. In schlieren experiment, the total dimensionless area of enclosed region I increases from 0.01 to 0.28. However, in the CFD simulations, the one of the enclosed region I increases from 0.32 to 0.60 and one of the enclosed region II increases from 0.06 to 0.26. Therefore, in spite of having similar growth trends, the total dimensionless area of the CFD simulated enclosed region measures considerably higher values, compared to the schlieren photography experiments.

#### 4. Discussion

In the current study, the outlines of vortex structures are three-dimensionally reconstructed from the schlieren photography images then projected on coordinate system planes to measure the vortex structure projection areas. Similarly, the CFD simulated vortex structures are projected on coordinate system planes to measure the vortex structures projection areas. As the coordinate systems are different between the experiment and CFD simulation, the total dimensionless areas of the projected vortex structures are therefore calculated and compared. In the down-stroke, although the simulated and experimentally captured vortex rings have similar magnitude of total dimensionless areas and similar development trend, the experimentally captured vortex ring has much faster rate of expansion compared to the CFD simulation results. In the up-stroke, the experimentally captured and numerically simulated vortex structures have similar development trends but

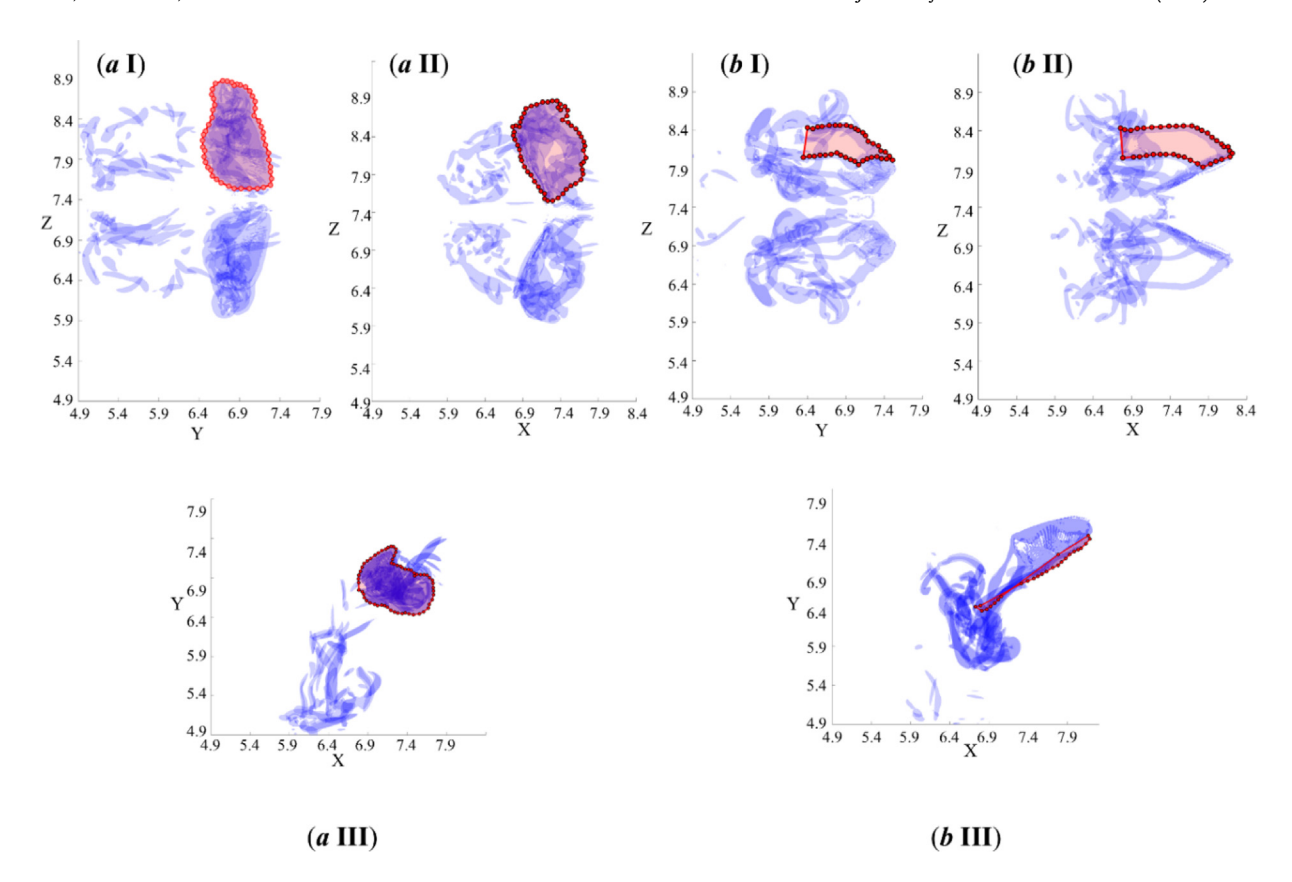


**Fig. 5.** Projections of vortex structures from CFD simulation. (a I, a III, a III) projections of down-stroke vortex loop structures on YZ, XZ, XY planes at t = 0.45 T. (b I, b III, b III) projections of up-stroke vortex structures on YZ, XZ, XY planes t = 1.0 T. Red dot lines highlight the areas of interesting vortex structures.

slightly different sizes. Particularly, the region enclosed by the vortices from the tips of fore- and hind-wings (region I) has considerably larger size in CFD simulation than the one in the experiments. These discrepancies might be related to the artificial viscosity implemented in the CFD simulation where the numerical simulation grid in the wake is not dense enough to resolve some turbulent structures and artificial viscosity is needed. Additionally, because the accurate wing kinematics and profiles cannot be extracted from the schlieren experiments due to the dark image of the hawkmoth wing and body, the experiment and simulation were actually conducted on two different hawkmoth individuals with different body weight and sizes (as compared in Table 1). Thus, differences in wing kinematics could exist between the experiments and simulations. Yet, since both analyses of vortex size in experiment and simulation were carried out on hawkmoths under the same hovering condition (lift force equals the body weight) with negligible body displacement, therefore both insects are expected having similar body and wing kinematics and the resulting flow structure will be similar except minor differences caused by the difference of Reynolds number (Reynolds number in experiment is approximately 6500, Reynolds number in CFD is approximately 7700).

In addition to perceiving the vortex structure sizes from estimating vortex structure projection areas, vortex structure projection area also command the aerodynamic force directly. On an enclosed structure of vortex ring, the aero/hydrodynamic force on moving surfaces can be estimated from knowing the size and strength of the vortex ring structure. Using Eq. (4), Dabiri analyzed and estimated the hydrodynamic force on a swimming *N. bachei.* (Dabiri, 2005)

$$F_T \approx \rho \boldsymbol{A} \frac{d}{dt}(\Gamma) + \rho \Gamma \frac{d}{dt}(\boldsymbol{A}) + \rho C_{ii} \frac{d}{dt} (\Omega_V \boldsymbol{U}_V)$$
(4)

In the right hand side of Eq. (4), the first term represents the aerodynamic force due to vortex loop strength  $(\Gamma)$  variation; the second term represents the aerodynamic force due to vortex loop area (A) variations; the third term represents the aerodynamic force due to added mass effect. Therefore, the aerodynamic force production is directly related to the vortex structure/loop projection area variation, thus our studies on enclosed vortex loop areas can be further utilized to estimate the aerodynamic force production on hovering hawkmoth. In a parallel study, a PIV experiment was conducted on a hovering hawkmoth to quantify the strength of the vortex loop in the down-stroke. With knowing both the vortex loop size and strength, the aerodynamic force was estimated, suggesting the vortex loop strength variation/flow unsteadiness plays a dominant role in aerodynamic force production. Furthermore, Eq. (4) justified the calculation of total dimensionless

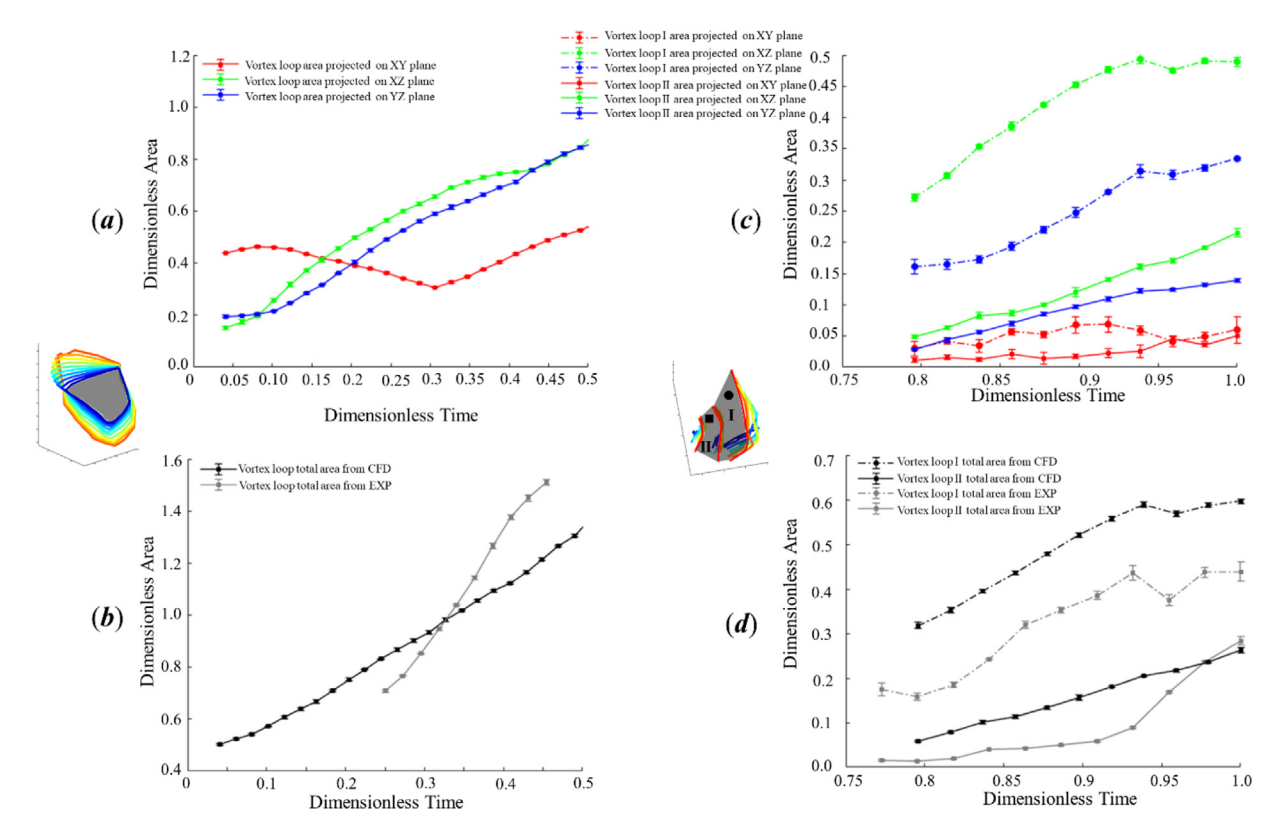


**Fig. 6.** Dimensionless areas of vortex structures from CFD simulation and comparison with experiment results. (a) Dimensionless areas of CFD simulated down-stroke vortex loop projected on YZ, XZ, XY planes. (b) Comparison of total dimensionless areas of the down-stroke vortex loop structures between the experiments and simulations. (c) Dimensionless areas of CFD simulated region I (edged on tip vortices from the hind- and fore-wing tips) projected on YZ, XZ, XY planes and Dimensionless areas of CFD simulated region II (edged on root and hind-wing tip vortices) projected on YZ, XZ, XY planes. (d) Comparison of total dimensionless areas of the region I and region II between the experiments and simulations.

area in Eq. (3), where the vortex loop area projections are treated as components of a vector. Thus the total dimensionless area of a vortex structure can be estimated by calculating the magnitude of the vector.

#### 5. Conclusion

In this paper, the three-dimensional vortex structure on a flying hawkmoth is reconstructed experimentally close to the wings where traditional volumetric flow visualization and measurement techniques cannot succeed because of laser projection and blockage of seeding particle imaging by insect wings/bodies. Also, a wake flow comparison between the experiment and CFD simulation is carried out on hovering hawkmoths, revealing good agreement between the schlieren photography experiments and IBM based CFD simulation. Utilizing the high-speed schlieren photography, the wake flow structure from a hovering hawkmoth was visualized and captured, depicting a vortex ring structure in the down-stroke and tip/root vortices during the up-stroke on each wing of the hovering hawkmoth. In CFD simulations, despite some minor difference about the secondary tip vortex in the down-stroke, similar vortex structure formations were numerically simulated and visualized comparing to the results from the experiment.

#### **CRediT authorship contribution statement**

**Yun Liu:** Conceptualization, Data analysis, Methodology, Writing – review & editing. **Angel David Lozano:** Data analysis, Writing. **Tyson L. Hedrick:** Software, Data collection, Writing – review & editing. **Chengyu Li:** Methodology, Writing – review & editing.

#### **Declaration of competing interest**

The authors declare that they have no known competing financial interests or personal relationships that could have appeared to influence the work reported in this paper.

#### Data availability statements

The data that support the findings of this study are available from the corresponding author upon request.

#### **Acknowledgments**

The hawkmoth experiments for running simulations were funded by National Science Foundation, USA (CPS-1239212) to T. L. Hedrick. The computational study was supported by the National Science Foundation, USA (CBET-2042368) and 2019 ORAU Ralph E. Powe Junior Faculty Enhancement Award to C. Li. All simulations were run on the High-Performance Computing Cluster of the College of Engineering at Villanova University.

#### Appendix A. Supplementary data

Supplementary material related to this article can be found online at https://doi.org/10.1016/j.jfluidstructs.2021. 103405.

#### References

Altshuler, D., Princevac, M., Pan, H., Lozano, J., 2009. Wake patterns of the wings and tail of hovering hummingbirds. Exp. Fluids 46, 835–846. Aono, Hikaru, Liang, Fuyou, Liu, Hao, 2008. Near- and far-field aerodynamics in insect hovering flight: an integrated computational study. J. Exp. Biol. 211, 239–257.

van den Berg, C., Ellington, C.P., 1997. The vortex wake of a 'hovering' model hawkmoth. Phil. Trans. R. Soc. London. Series B: Biological Sciences 352. 317–328.

Birch, J.M., Dickinson, M.H., 2001. Spanwise flow and the attachment of the leading-edge vortex on insect wings. Nature 412, 729-733.

Bomphrey, R.J., Lawson, N.J., Taylor, G.K., Thomas, A.L.R., 2006. Application of digital particle image velocimetry to insect aerodynamics: measurement of the leading-edge vortex and near wake of a Hawkmoth. Exp. Fluids 40, 546–554.

Bomphrey, R.J., Nakata, T., Phillips, N., Walker, S.M., 2017. Smart wing rotation and trailing-edge vortices enable high frequency mosquito flight. Nature 544, 92.

Bomphrey, R.J., Taylor, G.K., Thomas, A.L., 2009. Smoke visualization of free-flying bumblebees indicates independent leading-edge vortices on each wing pair. Exp. Fluids 46, 811–821.

Chen, L., Wu, J., Cheng, B., 2020. Leading-edge vortex formation and transient lift generation on revolving wing at low Reynolds number. Aerosp. Sci. Technol. 97.

Cheng, B., Roll, J., Liu, Y., Troolin, D.R., Deng, X., 2014. Three-dimensional vortex wake structure of flapping wings in hovering flight. J. R. Soc. Interface 11, 20130984.

Dabiri, J.O., 2005. On the estimation of swimming and flying forces from wake measurements. J. Exp. Biol. 208, 3519–3532.

Ellington, C.P., vandenBerg, C., Willmott, A.P., Thomas, A.L.R., 1996. Leading-edge vortices in insect flight. Nature 384, 626-630.

Hedrick, T.L., 2008. Software techniques for two- and three-dimensional kinematic measurements of biological and biomimetic systems. Bioinspiration Biomim. 3, 034001.

Henningsson, P., Michaelis, D., Nakata, T., Schanz, D., Geisler, R., Schröder, A., et al., 2015. The complex aerodynamic footprint of desert locusts revealed by large-volume tomographic particle image velocimetry. J. R. Soc. Interface 12, 20150119.

Jardin, T., 2017. Coriolis effect and the attachment of the leading edge vortex. J. Fluid Mech. 820.

Kim, D., Gharib, M., 2010. Experimental study of three-dimensional vortex structures in translating and rotating plates. Exp. Fluids 49, 329–339.

- Li, Chengyu, 2020. Effects of wing pitch kinematics on both aerodynamic and olfactory functions in an upwind surge. Proc. Inst. Mech. Eng. C 0954406220907950.
- Li, Chengyu, Dong, Haibo, 2016. Three-dimensional wake topology and propulsive performance of low-aspect-ratio pitching-rolling plates. Phys. Fluids 28.7. 071901.
- Li, C., Dong, H., 2017a. Wing kinematics measurement and aerodynamics of a dragonfly in turning flight, Bioinspiration Biomim. 12, 026001.
- Li, Chengyu, Dong, Haibo, 2017b. Wing kinematics measurement and aerodynamics of a dragonfly in turning flight. Bioinspiration Biomim. 12.2, 026001.
- Li, Chengyu, Dong, Haibo, Liu, Geng, 2015. Effects of a dynamic trailing-edge flap on the aerodynamic performance and flow structures in hovering flight. J. Fluids Struct. 58, 49–65.
- Li, Chengyu, Dong, Haibo, Zhao, Kai, 2018. A balance between aerodynamic and olfactory performance during flight in Drosophila. Nature Commun. 9.1, 1–8.
- Li, C., Dong, H., Zhao, K., 2018a. A balance between aerodynamic and olfactory performance during flight in drosophila. Nature Commun. 9, 1-8.
- Li, Chengyu, et al., 2017. Computational modeling and validation of human nasal airflow under various breathing conditions. J. Biomech. 64, 59–68. Liu, Y., Cheng, B., Barbera, G., Troolin, D.R., Deng, X., 2013. Volumetric visualization of the near-and far-field wake in flapping wings. Bioinspiration Biomim. 8, 036010.
- Liu, G., Dong, H., Li, C., 2016. Vortex dynamics and new lift enhancement mechanism of wing–body interaction in insect forward flight. J. Fluid Mech. 795. 634–651.
- Liu, H., Ellington, C.P., Kawachi, K., Van den Berg, C., Willmott, A.P., 1998. A computational fluid dynamic study of hawkmoth hovering. J. Exp. Biol. 201. 461–477.
- Liu, Y., Roll, J., Van Kooten, S., Deng, X., 2018. Schlieren photography on freely flying hawkmoth. Biol. Lett. 14, 20180198.
- Mittal, R., Dong, H., Bozkurttas, M., Najjar, F.M., Vargas, A., von Loebbecke, A., 2008. A versatile sharp interface immersed boundary method for incompressible flows with complex boundaries. J. Comput. Phys. 227, 4825–4852.
- Mittal, R., Iaccarino, G., 2005b. Immersed boundary methods. Annu. Rev. Fluid Mech. 37, 239–261.
- Muijres, F.T., Johansson, L.C., Barfield, R., Wolf, M., Spedding, G.R., Hedenstrom, A., 2008. Leading-edge vortex improves lift in slow-flying bats. Science 319, 1250–1253.
- Nakata, T., Liu, H., 2012. Aerodynamic performance of a hovering hawkmoth with flexible wings: a computational approach. Proc. R. Soc. Lond. Ser. B: Biol. Sci. 279, 722–731.
- Pournazeri, S., Segre, P.S., Princevac, M., Altshuler, D.L., 2013. Hummingbirds generate bilateral vortex loops during hovering: evidence from flow visualization. Exp. Fluids 54, 1439.

Sane, S.P., 2003. The aerodynamics of insect flight. J. Exp. Biol. 206, 4191-4208.

Schanz, D., Gesemann, S., Schröder, A., 2016. Shake-the-box: Lagrangian particle tracking at high particle image densities. Exp. Fluids 57, 70.

Shyy, W., Aono, H., Chimakurthi, S.K., Trizila, P., Kang, C.K., Cesnik, C.E.S., et al., 2010. Recent progress in flapping wing aerodynamics and aeroelasticity. Prog. Aerosp. Sci. 46, 284–327.

Smits, A.J., Lim, T.T., 2012. Flow Visualization: Techniques and Examples. Imperial College Press, London, UK.

Varfvinge, K., Johansson, L., Hendenström, A., 2021. Hovering flight in hummingbird hawkmoths: kinematics, wake dyanmics and aerodynamic power. J. Exper. Biol. 224 (10), 1–16.

Viderler, J., Stamhuis, E., Povel, G., 1996. Leading-edge vortices in insect flight. Nature 384.

Wan, H., Dong, H., Gai, K., 2015. Computational investigation of cicada aerodynamics in forward flight. J. R. Soc. Interface 12, 20141116.

Wang, J., Ren, Y., Li, C., Dong, H., 2019. Computational investigation of wing-body interaction and its lift enhancement effect in hummingbird forward flight. Bioinspiration Biomim. 14, 046010.

Warrick, D.R., Tobalske, B.W., Powers, D.R., 2005. Aerodynamics of the hovering hummingbird. Nature 435, 1094-1097.